International Journal of Heat and Mass Transfer 61 (2013) 565–576

Contents lists available at SciVerse ScienceDirect

International Journal of Heat and Mass Transfer

journal homepage: www.elsevier.com/locate/ijhmt

Chaotic flow in a 2D natural convection loop with heat flux boundaries

William F. Louisos [a,b,*], Darren L. Hitt [a,b], Christopher M. Danforth [a,c]

[a] College of Engineering & Mathematical Sciences, The University of Vermont, Votey Building, 33 Colchester Avenue, Burlington, VT 05405, United States
[b] Mechanical Engineering Program, School of Engineering, The University of Vermont, Votey Building, 33 Colchester Avenue, Burlington, VT 05405, United States
[c] Department of Mathematics & Statistics, Vermont Complex Systems Center, Vermont Advanced Computing Core, The University of Vermont, Farrell Hall, 210 Colchester Avenue, Burlington, VT 05405, United States

ARTICLE INFO

Article history:
Received 13 August 2012
Received in revised form 1 February 2013
Accepted 3 February 2013

Keywords:
Thermosyphon
Natural convection
Unstable convection
Lorenz-like chaos
Rayleigh number

ABSTRACT

This computational study investigates the nonlinear dynamics of unstable convection in a 2D thermal convection loop (i.e., thermosyphon) with heat flux boundary conditions. The lower half of the thermosyphon is subjected to a positive heat flux into the system while the upper half is cooled by an equal-but-opposite heat flux out of the system. Water is employed as the working fluid with fully temperature dependent thermophysical properties and the system of governing equations is solved using a finite volume method. Numerical simulations are performed for varying levels of heat flux and varying strengths of gravity to yield Rayleigh numbers ranging from 1.5×10^2 to 2.8×10^7. Simulation results demonstrate that multiple regimes are possible and include: (1) conduction, (2) damped, stable convection that asymptotes to steady-state, (3) unstable, Lorenz-like chaotic convection with flow reversals, and (4) high Rayleigh, aperiodic stable convection without flow reversals. Delineation of the various flow regimes, as characterized by the temporal evolution of bulk mass flow rate, is obtained in terms of heat flux, gravity, and the Rayleigh number. Temporal frequencies of the oscillatory behavior and residence time in a circulatory direction are explored and described for the various thermal and gravitational forcing (Rayleigh number) applied to the system.

1. Introduction

There exist many phenomena of interest to the geophysics and engineering communities that are driven by buoyancy and natural convection. Examples of natural convection systems occurring on geophysical scales and in the Earth's environment include: mesoscale convective thunderstorms that can result in damaging and costly wind events such as derechos [1,2], downbursts, and straight-line wind-storms depicted as a classic 'bow echo' on radar [3]; land and sea breezes as a result of differential heating between landmass and an adjacent body of water; mantle convection of the Earth's asthenosphere which results in the creeping motion of the lithosphere, plate tectonics, and volcanic activity; and Hadley cells in Earth's atmosphere which relate to large scale motions of the jet stream and Rossby waves. Examples of natural convection cells occurring in engineering devices include solar water heaters, nuclear reactors, and gas turbine blade cooling among many others [4–6].

The nonlinear dynamics of unstable convection were studied in a simple model by Edward Lorenz in his 1963 paper "Deterministic Nonperiodic Flow". Indeed, his differential equation model for natural convection in a Rayleigh–Bénard cell has been widely employed to developed improved forecasting methodologies for mathematical models of the Earth's atmosphere [8]. For example, meteorologists use ensemble forecasting and teleconnection indices – such as the North Atlantic Oscillation Index (NAO) which pertains to North-East US weather patterns, – in order to quantify the oscillatory and chaotic fluctuations of the jet stream in an attempt to better understand weather patterns and provide medium range forecasting with improved accuracy.

Physical and/or numerical models such as thermal convection loops, or "thermosyphons", are a simplified geometry that represents a viable tool for studying the behavior of natural convection [8]. Thermosyphons are a useful construct for performing scientific studies as they limit convection to a single, large cell and thus provide the simplest physical model which allows for examination of the various flow regimes.

Thermosyphons are fluid systems in which flow is induced via buoyancy forces that occur when unstable temperature gradients exist within the system (i.e., heating from the bottom and cooling from the top). The fluid circulates within a closed, circular tube a torus that is oriented vertically in space with respect to gravity

* Corresponding author at: Department of Mechanical Engineering, School of Engineering, The University of Vermont, Votey Building, 33 Colchester Avenue, Burlington, VT 05405, United States.

E-mail addresses: william.louisos@uvm.edu (W.F. Louisos), darren.hitt@uvm.edu (D.L. Hitt), chris.danforth@uvm.edu (C.M. Danforth).

0017-9310/$ - see front matter © 2013 Elsevier Ltd. All rights reserved.
http://dx.doi.org/10.1016/j.ijheatmasstransfer.2013.02.015

Nomenclature

CCW	counter-clockwise
c_p	constant pressure specific heat (kJ/(kg · K))
CW	clockwise
e	specific internal energy (kJ)
$f_{\max}$	dominant frequency (Hz)
g	gravitational acceleration
h	convection coefficient (W/(m · K))
I	identity matrix
k	thermal conductivity (W/(m · K))
L	characteristic length scale (m)
$\dot{m}$	mass flow rate (kg/s)
p	pressure (Pa)
q''	heat flux (±W/m²)
Ra	Rayleigh number
T	static temperature (K)
t	time (s)
$\mathbf{V}$	velocity vector (m/s)
α	thermal diffusivity (m²/s)
β	thermal expansion coefficient (1/K)
θ	azimuth coordinate (rads)
τ	viscous stress tensor (Pa)
ν	kinematic viscosity (m²/s)
μ	dynamic viscosity (kg/(m² · s))
ρ	density (kg/m³)

while it is heated from the bottom and cooled from the top. The resulting thermal gradient may yield quiescent conduction, or, if the gradient is sufficiently large, to buoyancy driven convection. Thermosyphons exhibit many typical nonlinear convective effects wherein multiple flow regimes are possible based on the operating parameters of a particular thermosyphon system. The various flow regimes are typically delineated as (1) pure conduction and/or quasi-conduction, (2) stable convection with unidirectional flow, (3) unstable, Lorenz-like chaotic convection with flow reversals characterized by bulk fluid motion alternating from clockwise *CW* to counter-clockwise *CCW* (and/or vice versa) flow around the thermosyphon, and (4) high-Rayleigh, aperiodic, stable convection without flow reversals.

Comprehensive review articles written by Yang et al. [9], Raithby and Hollands [10], and Jaluria [11] discuss several important enclosure problems in various branches of engineering, geophysics, environmental sciences. The articles [4–11] report a wealth of theoretical and experimental studies of this simple system, which exhibits typical nonlinear convective effects. Earlier thermosyphon studies employed 1D models in order to study flow behavior in a thermosyphon with the assumption that all governing parameters are uniform over any given cross section at any moment in time [12,13]. Periodic oscillations were found analytically by Keller [12] in a 1D model consisting of a fluid-filled tube bent into a rectangular shape and standing in a vertical plane. Gorman et al. [14] presented a quantitative comparison of the flow in a thermosyphon with the nonlinear dynamics of the Lorenz model. Here the system was heated with constant flux over the bottom half and cooled isothermally over the top half. The boundaries of different flow regimes were delineated experimentally and the characteristics of chaotic flow regimes were discussed in relation to the Lorenz model. Several flow stability studies have been performed by Vijayan [15], Jiang et al. [16], and Jiang and Shoji [17] while Desrayaud et al. [18] completed a numerical investigation of unsteady, laminar natural convection in a 2D thermosyphon driven by a constant heat flux over the bottom half and cooled isothermally over the top half. For a particular range of forcing (i.e., Rayleigh number), it has been observed that the bulk fluid motion in a thermosyphon is chaotic and undergoes flow reversals. Creveling et al. [19] proposed a positive feedback mechanism in order to explain these flow reversals in a thermosyphon.

Despite the large body of literature pertaining to thermosyphons, only minimal information exists regarding the spatiotemporal behavior of the flow-field within a thermosyphon. The thermal structure of the flow and velocity-field were characterized in time by Ridouane et al. [20,21] where they examine isothermal boundary conditions in 2D and 3D thermosyphons. It was found that for 2D thermosyphons, chaotic flow regimes and the associated flow reversals occur for Rayleigh numbers $9.5 \times 10^4 < Ra < 4.0 \times 10^5$. However, in the 3D isothermal work [21], flow reversals where not observed for Rayleigh numbers ranging from $10^3 < Ra < 2.3 \times 10^7$. Ridouane et al. suggest that 3D flow structures increase flow resistance and thus dampen the flow instability mechanism responsible for bulk flow reversals observed in 2D thermosyphons. The details describing the mechanism by which this damping occurs are not described.

The motivation for exploring the heat flux boundary condition in the present work is to investigate a more realistic scenario; simulations of the flux boundary condition allow for better comparisons with actual laboratory experiments. In addition, flow reversals were not observed in 3D isothermal simulations, but are known to occur in experiments with heat flux boundaries. The present study considers simulations of 2D thermosyphons with iso-heat flux boundaries: heating on the bottom-half of the loop ($+q''$) and an equal but opposite iso-heat flux cooling on the

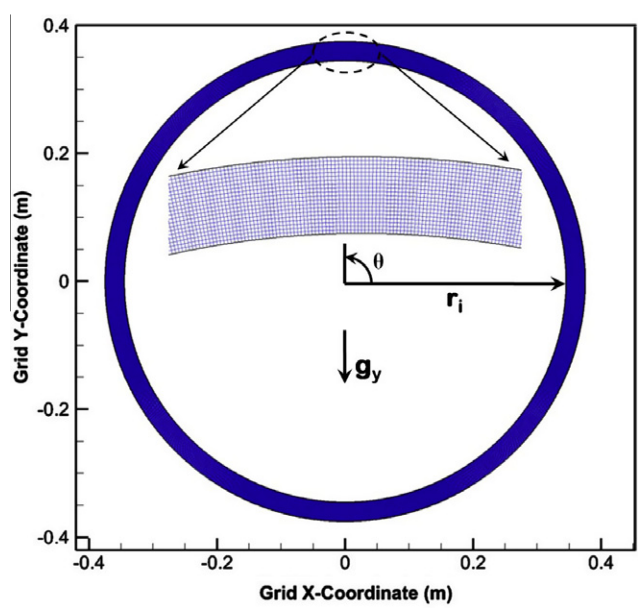

Fig. 1. The 2D computational mesh used throughout this study. The inset shows a zoomed-in view of the top section of the mesh as indicated by the dashed circle. The dimensions of the thermosyphon are r_i = 34.5 cm inner radius and r_o = 37.5 cm outer radius. The lower half of the loop ($\pi < \theta < 2\pi$) is imposed with an iso-heat-flux into the system while the upper half ($0 \leqslant \theta \leqslant \pi$) is imposed with an equal and opposite iso-heat-flux out of the system.

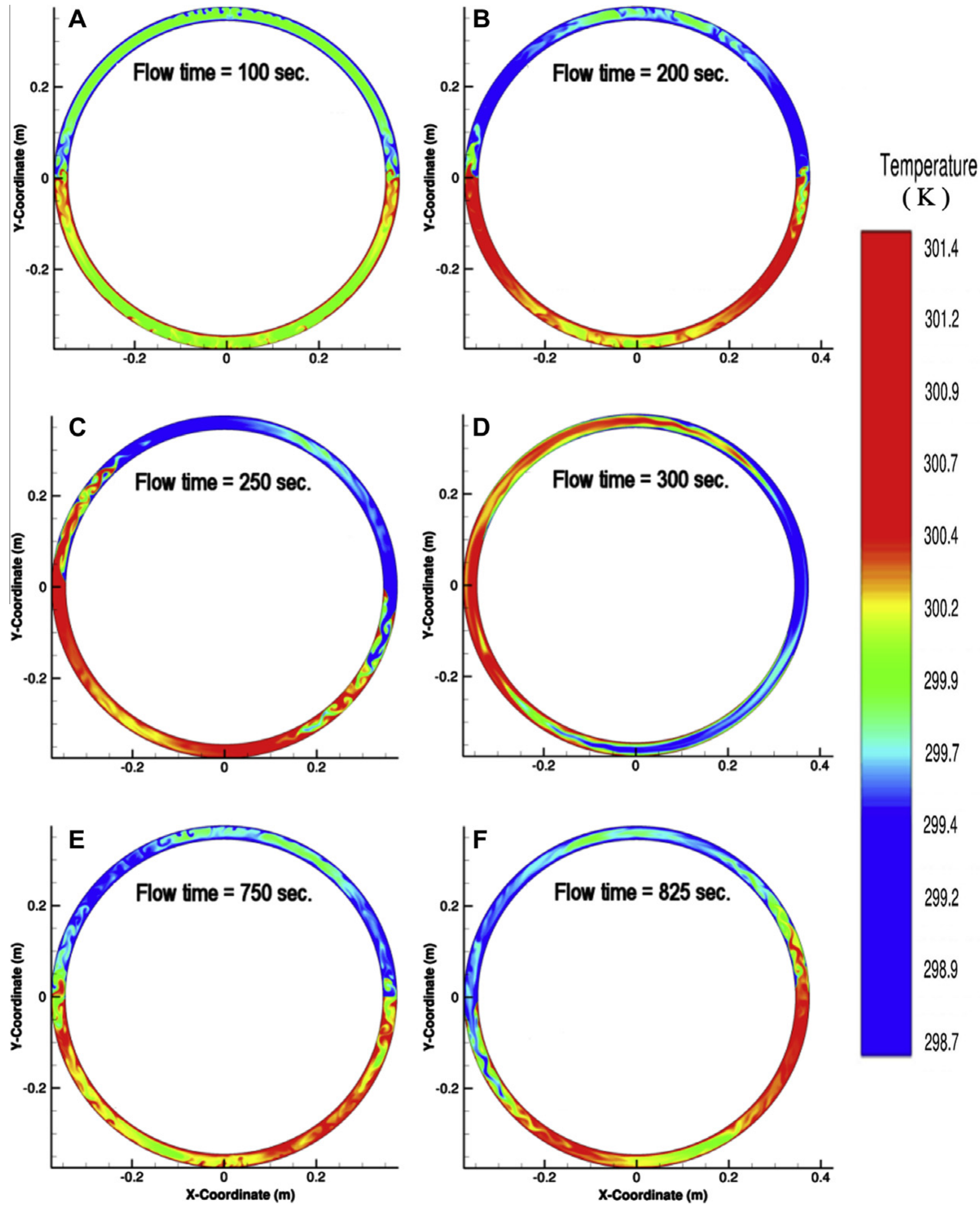

Fig. 2. The time evolution of the temperature contours in the thermosyphon (A–F). In figure (A), the temperature gradient is beginning to increase and flow instabilities can be seen at $\theta = 0$ and $\theta = \pi$. In figure (B), initiation of clockwise flow can be seen. Figures (C) and (D) show established clockwise flow while figure (E) shows the temperature field at the moment of flow reversal from clockwise to counter-clockwise. In figure (F), counter-clockwise flow has been established. This is the typical behavior of a flow reversal. Here gravity is 9.8 m/s^2 and the heat flux is ±200 W/m^2 which yields a Rayleigh number of $Ra \sim 5.7 \times 10^6$.

top half ($-q''$). Special care is devoted to determining the flow regimes that are encountered as the Rayleigh number is increased from 1.45×10^2 to 2.83×10^7. We also seek to delineate the various flow regimes in a gravity/heat flux parametric space while examining both the temporal evolution and the *RMS* value of the bulk mass flow rate in the thermosyphon. Particular focus is placed on characterizing flow reversals as defined by the transition from clockwise *CW* to counter-clockwise *CCW* (or vice versa) flow around the thermosyphon.

2. Model of physical system

The physical system for this problem, depicted in Fig. 1, consists of a circular closed-loop filled with liquid water at atmospheric

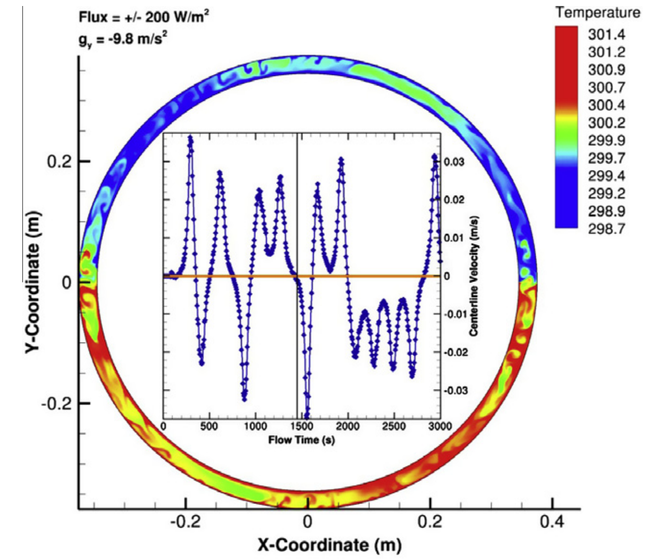

Fig. 3. An illustration of the temperature contours in the thermosyphon at the moment of flow transition from *CW* to *CCW* as indicated by the vertical line at time $t = 1{,}450$ s in the centerline velocity vs. time plot. Here the forcing is identical to that shown in Fig. 2. Animated movies of flow simulations for a range of Rayleigh numbers are available as supplemental material.

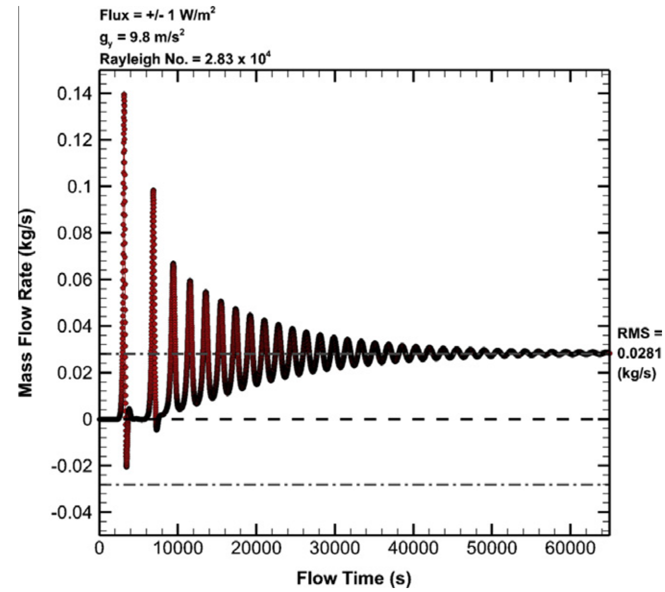

Fig. 4. The temporal evolution of mass flow rate in the thermosyphon at a Rayleigh number of $Ra \sim 2.83 \times 10^4$. This flow regime is characterized as damped, stable convection as the oscillations remain *CW* and decay to the *RMS*, steady-state value.

pressure and oriented in a vertical plane like a wheel with the force of gravity in the $-y$ direction. The physical dimensions of the loop are 69 cm inner diameter and 75 cm outer diameter. Initially, the water is at rest ($\mathbf{V} = 0$) throughout the domain and in thermal equilibrium at $T_0 = 300$ K. In order to initiate natural convection within the closed space, both the inner and outer upper walls ($\theta = 0$ to π) are imposed with a heat flux ($-q''$) out of the system while both the inner and outer lower walls ($\theta = \pi$ to 2π) are imposed with an equal in magnitude but opposite direction heat flux ($+q''$) into the system. The equal and opposite heat fluxes are held constant along with the acceleration of gravity while the fluid system is monitored as it evolves in time.

In this study, our focus is the delineation of natural convection flow regimes for varying magnitudes of heat flux and gravity as characterized by the Rayleigh number. The Rayleigh number seeks to capture the relative strength of buoyancy as compared to viscous forces multiplied by the ratio of momentum and thermal diffusivity for thermally driven fluid systems. The Rayleigh number is traditionally defined as

$$Ra = \frac{\rho g \beta \Delta T L^3}{\mu \alpha} \tag{1}$$

where ρ is the fluid density (kg/m^3), g is the acceleration of gravity (m/s^2), β is the thermal expansion coefficient (1/K), ΔT is the temperature difference between the hot a cold boundaries (K), L is the characteristic length scale (m), μ is the dynamic viscosity (kg/(m $\cdot$ s)), and α is the thermal diffusivity (m^2/s). In this study of heat flux boundary conditions (as opposed to isothermal boundaries), various combinations of flow parameters (e.g., gravity and heat flux) may yield identical Rayleigh numbers. In other words, a unique set of flow parameters does not exist for a particular Rayleigh number. While the Rayleigh number formulation of Eq. (1) is readily employed for isothermal boundary conditions, it must be modified in order to account for the expected non-isothermal heat flux boundaries in this work. For the case of heat flux boundary conditions, a characteristic temperature differential is required to compute the Rayleigh number. To obtain a representation of the temperature differential, we appeal to Fourier's law of heat conduction

$$q'' = k \frac{\Delta T}{L} \tag{2}$$

in order to estimate temperature difference ΔT in terms of the heat flux q'' (W/m^2) and thermal conductivity k (W/(m $\cdot$ K)). This readily provides a redefinition of the Rayleigh number in a form appropriate for the heat flux boundary condition. As such, with $\Delta T = q''L/k$, the resulting Rayleigh number formulation used throughout this work is

$$Ra = \frac{\rho g \beta L^4}{\mu \alpha k} q''. \tag{3}$$

Table 1
A summary of temperature anomalies, the associated buoyant forcing direction, and the change in forcing strength as a function of position within the thermosyphon.

Location in thermosyphon	Heat flux	Anomalous fluid pocket	Direction of buoyant forcing	Change in forcing magnitude
$0 < \theta < \pi/2$	Cooling	Hot	*CCW*	Decrease
		Cold	*CW*	Increase
$\pi/2 < \theta < \pi$	Cooling	Hot	*CW*	Decrease
		Cold	*CCW*	Increase
$\pi < \theta < (3\pi)/2$	Heating	Hot	*CW*	Increase
		Cold	*CCW*	Decrease
$(3\pi)/2 < \theta < 0$	Heating	Hot	*CCW*	Increase
		Cold	*CW*	Decrease

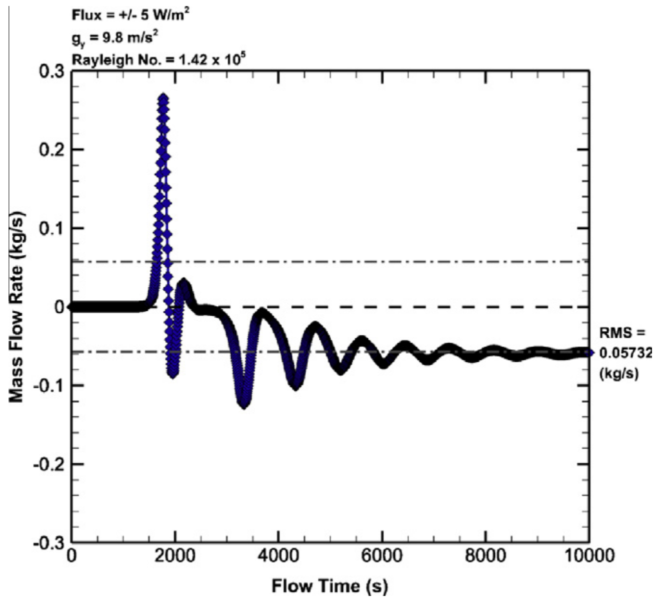

Fig. 5. The temporal evolution of mass flow rate in the thermosyphon at a Rayleigh number of $Ra \sim 1.42 \times 10^5$. The flow undergoes two initial, transient flow reversals during start-up and then damps out as steady *CCW* convection is established at a mass flow rate of approximately 0.06 kg/s.

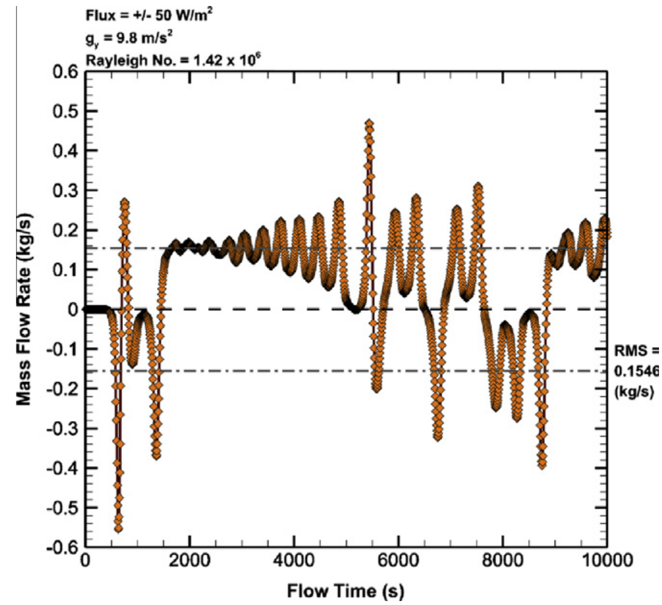

Fig. 7. The temporal evolution of mass flow rate in the thermosyphon at a Rayleigh number of $Ra \sim 1.42 \times 10^6$. The flow undergoes initial, transient flow reversals during start-up, oscillations then begin small and grow large until a flow reversal occurs and a fully chaotic flow regime is established.

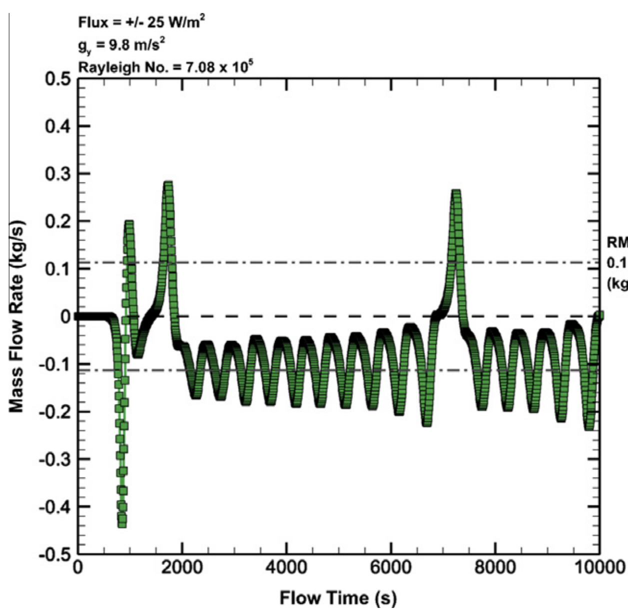

Fig. 6. The temporal evolution of mass flow rate in the thermosyphon at a Rayleigh number of $Ra \sim 7.08 \times 10^5$. The flow undergoes four initial, transient flow reversals before settling into a state of growing, *CCW* oscillations which then experience flow reversals after the oscillations have grown sufficiently large.

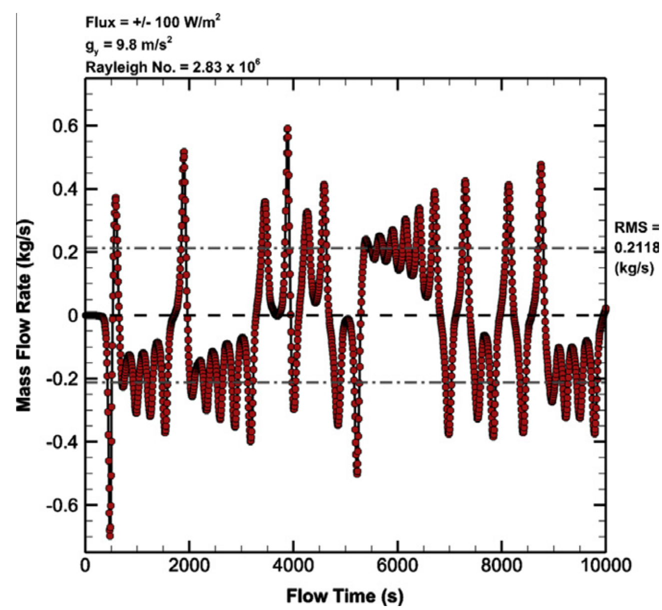

Fig. 8. The temporal evolution of mass flow rate in the thermosyphon at a Rayleigh number of $Ra \sim 2.83 \times 10^6$. The flow undergoes initial, transient flow reversals and quickly establishes a chaotic flow regime characterized by growing oscillations with an unpredictable number of cycles before a flow reversal is observed.

Variations of the Rayleigh number are achieved by adjusting the value of the heat flux ($0.1 \leqslant q'' \leqslant 1000\ \mathrm{W/m^2}$) and the gravitational acceleration ($0.5 \leqslant g \leqslant 9.8\ \mathrm{m/s^2}$) in order to yield Rayleigh numbers ranging from $1.45 \times 10^2 \leqslant Ra \leqslant 2.83 \times 10^7$.

3. Computational methods

Liquid water at an operating pressure of one atmosphere (101.325 kPa) is the working fluid in all simulations. All thermophysical properties, including density (ρ), specific heat c_p, thermal conductivity (k), and dynamic viscosity (μ), are modeled as temperature dependent via a piecewise linear function that includes 31 data points spanning beyond the temperature range of the water in the thermosyphon.

The computational domain is based on the geometry described above and has been generated using Fluent Inc.'s Gambit grid generation software [22]. An example of the grid is provided in Fig. 1 with an inset showing a detailed view of the mesh in the top portion of the thermosyphon. A formal grid-independence study has been performed as described in Ridouane et al. [20] and the final mesh contains 31,400 uniform, orthogonal, quadrilateral finite vol-

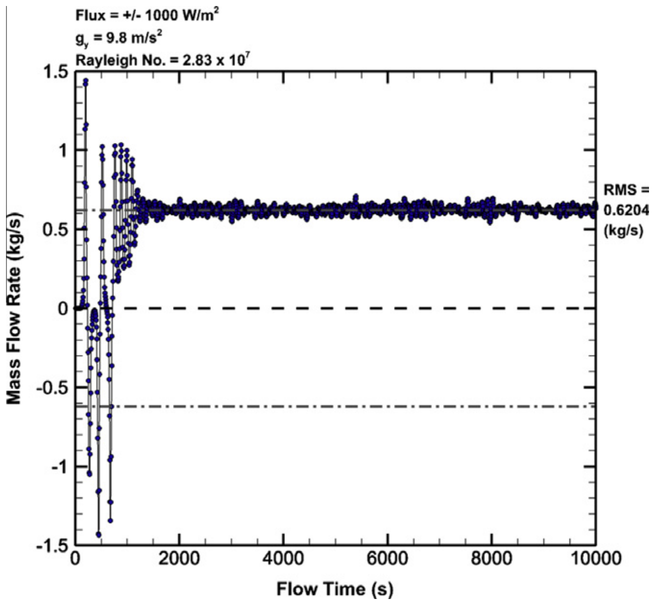

Fig. 9. The temporal evolution of mass flow rate in the thermosyphon at a Rayleigh number of $Ra \sim 2.83 \times 10^7$. The flow undergoes several initial, transient flow reversals before establishing a steady, high-Rayleigh, aperiodic, stable convective flow regime with small amplitude, high frequency oscillations centered on a mass flow *RMS* of approximately 0.525 kg/s.

umes with no symmetry assumption. The flow field is governed by the conservation of mass, momentum, and energy according to

$$\frac{\partial}{\partial t}(\rho) + \nabla \cdot (\rho \mathbf{V}) = 0 \tag{4}$$

$$\frac{\partial}{\partial t}(\rho \mathbf{V}) + \nabla \cdot (\rho \mathbf{V}\mathbf{V}) = -\nabla p + \rho(T)g + \nabla \cdot \tau \tag{5}$$

$$\frac{\partial}{\partial t}(\rho e) + \nabla \cdot (\rho \mathbf{V} e) = \nabla \cdot (k\nabla T + (\tau \cdot \mathbf{V})) \tag{6}$$

$$e = c_p T + \frac{1}{2}|\mathbf{V}|^2 \tag{7}$$

$$\tau = \mu\left((\nabla \mathbf{V} + \nabla \mathbf{V}^T) - \frac{2}{3}\nabla \cdot \mathbf{VI}\right) \tag{8}$$

where e is the specific internal energy, c_p is the specific heat at constant pressure, and τ is the Newtonian viscous stress tensor. The no-slip velocity boundary condition is imposed on the inner and outer walls of the computational domain. Owing to the low flow velocities and Reynolds numbers, a laminar viscous model is employed without viscous heating.

The governing equations are solved numerically using the finite volume method (FLUENT 6.3 [22]). An implicit, pressure-based, segregated solver is employed and all discretization schemes are of second-order accuracy or higher. The QUICK scheme is used for the momentum and energy discretization while the Green–Gauss scheme is used for the spatial discretization. The pressure discretization employs the body-force weighted model and pressure–velocity coupling is handled by the SIMPLE pressure correction algorithm.

In this work, we seek to resolve the temporal evolution of the flow-field from an initial condition of thermal equilibrium at T_0 = 300 K and zero velocity throughout the domain. The unsteady numerical model is second-order implicit in time and utilizes a time-step size of Δt = 0.25 s which is small enough to render the solution insensitive to time-stepping. Convergence at each time-step is assessed via computed residuals (mass, momentum, and energy) and flow monitors (e.g. $\dot{m}$, T) at key locations within the domain. The solution at a given time-step is deemed converged when the numerical residuals have fallen below 10^{-5} and flow monitors change by less than 0.01% with further iterations. In this work, we numerically simulate the first $\geqslant$10,000 s of flow time (40,000 time-steps) in order to analyze flow-field from start-up at time t = 0 (i.e., quiescent, thermal equilibrium throughout the domain at a temperature of 300 K) to the point where the flow regime is able to be well characterized ($\geqslant$10,000 s).The efficacy of this computational strategy as it pertains to this model of the thermosyphon has been demonstrated in previous work [20].

4. Results and discussion

In this section, we present and discuss the numerical results from natural convection simulations in the thermosyphon. First, illustrations are presented to orient the reader with respect to typical flow regimes and temperature fields. Next, the *RMS* value of mass flow pulsations is computed with respect to the Rayleigh number in order to quantify bulk fluid flow as a function of the forcing in the system. We then delineate the transition sequence across flow regimes as the Rayleigh number and the associated forcing is increased. Finally, we close this section with a summary and delineation of flow regimes for the range of operating parameters considered in this work.

4.1. Overview of flow field characteristics

As a point of illustration and orientation for the reader, we first present in Fig. 2 several instantaneous snap-shots of temperature contours showing the establishment of an initial temperature gradient followed by initiation of clockwise flow. Clockwise flow is then followed by a flow reversal to counter-clockwise flow. The temporal evolution of the flow in Fig. 2 is (A)–(F) for which gravity is set to 9.8 m/s^2 and the wall heat flux is =±200 W/m^2 yielding a Rayleigh number of $Ra \sim 5.7 \times 10^6$. (Animated movies of flow simulations for a range of Rayleigh numbers are available as supplemental material.)

Fig. 3 shows a snap-shot of the temperature field at the moment of a typical flow reversal with forcing of $Ra \sim 5.7 \times 10^6$. Also shown in Fig. 3(inset) is a plot of the temporal evolution of the centerline flow velocity where (+) velocity is clockwise. A flow reversal can be seen on the inset velocity plot as the curve crosses from positive (*CW*) to negative (*CCW*) centerline velocity as indicated by the vertical line at a flow-time of 1450 s. This flow regime is characterized as chaotic convection with repeating flow reversals. In Fig. 3, the temperature field and shearing flow patterns resemble Kelvin–Helmholtz instabilities. These instability patterns are especially prominent in the vicinity of the heat flux discontinuity (i.e., at θ = 0 and $\theta = \pi$) where the boundary condition of positive and negative heat flux juxtapose.

Several growing oscillations of the average bulk velocity, and consequently the associated mass flow rate in the thermosyphon, are observed in the inset of Fig. 3 between 2000 and 2700 s. The oscillations are a unidirectional pulsation of the flow magnitude. If the oscillations grow sufficiently large, the flow will reverse direction from *CCW* to *CW* (or vice versa if the oscillations were originally in the *CW* direction). To be clear, oscillatory behavior does not necessitate a flow reversal. Rather, it is growing oscillations that may lead to flow reversals whereas decaying oscillations often yield to stable, steady convection.

An explanation of fluid instability and the positive feedback mechanism that generates the observed flow reversals has been previously discussed by Creveling et al. [19]. The mechanism by which buoyant forcing changes as the flow rotates and/or oscillates

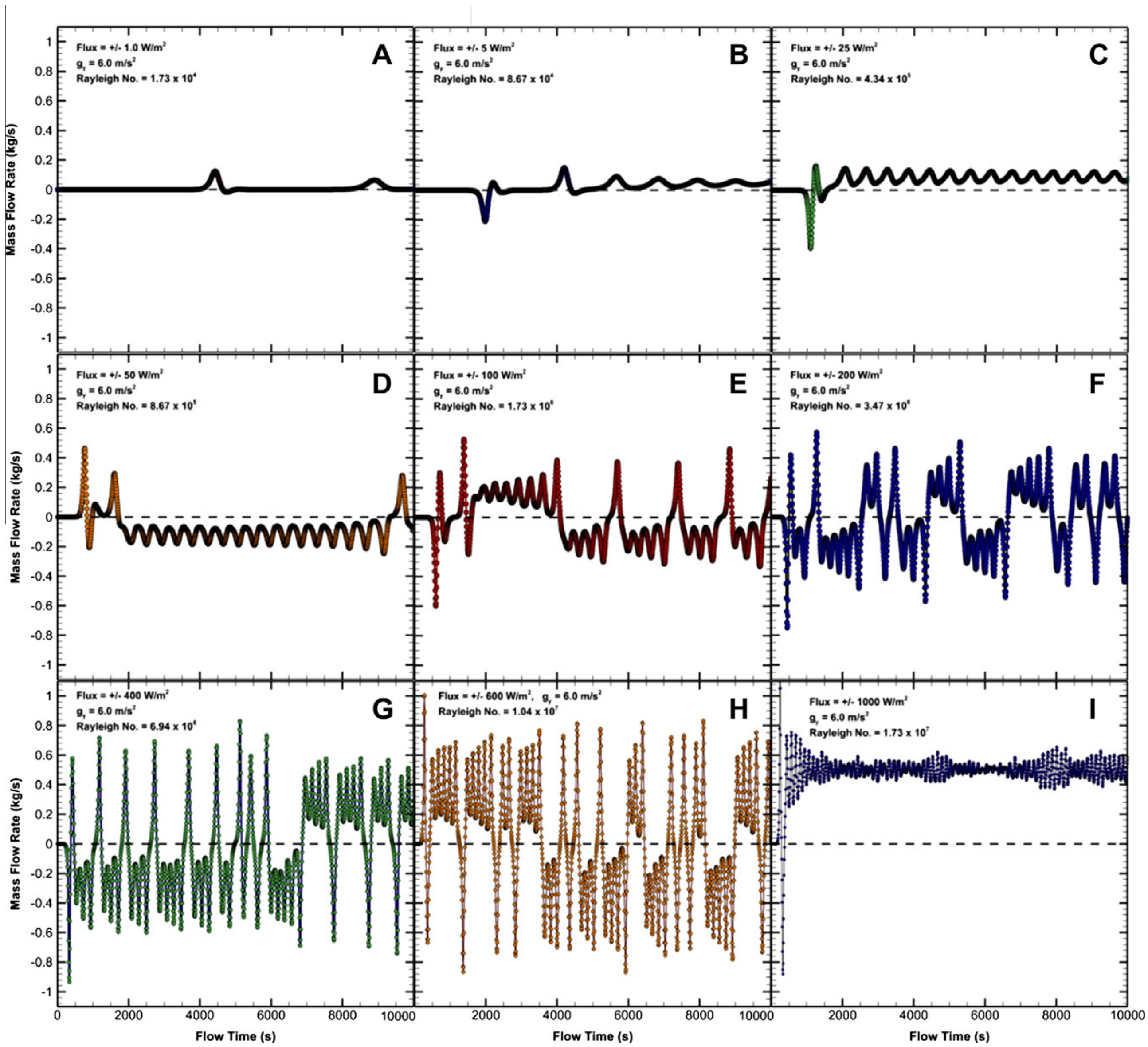

Fig. 10. A summary figure showing the bulk mass flow rate as a function of flow time in the convection loop for increasing Rayleigh number (A–I) with heat flux (1.0 W/m^2 < $\pm q''$ < 1000 W/m^2) while operating with a gravitational constant of g_y = 6.0 m/s^2. For comparison purposes, the mass flow rate axes are shown for a constant range in each plot.

in the thermosyphon is as follows: Flow instabilities occurring at $\theta = 0$ and $\theta = \pi$ produce anomalous hot and cold pockets that are able to move around and/or propagate within the thermosyphon. The particular location(s) of the anomalous pocket(s) result in either *CW* or *CCW* buoyant forcing. For example, a hot fluid pocket located between $(3\pi)/2 < \theta < \pi/2$ and/or a cold fluid pocket located between $\pi/2 < \theta < (3\pi)/2$ both generate *CCW* buoyant forcing.

As the flow in the thermosyphon rotates and/or oscillates, the magnitude and direction of the buoyant forcing evolves as anomalous thermal pockets traverse the thermosyphon and either absorb or reject heat based on the particular location of said anomalies. For example, a hot fluid pocket found between $(3\pi)/2 < \theta < 0$ is further heated and thus *increases* buoyant forcing in the *CCW* direction whereas a cold fluid pocket found between $0 < \theta < \pi/2$ is further cooled and thus *decreases* forcing in the *CCW* direction (or, equivalently, *increases* forcing in the *CW* direction). In general, if an anomalous hot region of fluid is heated, the buoyant force increases, and if a hot pocket of fluid is cooled, the forcing decreases. Table 1 provides a complete summary of the possible forcing scenarios and the change in forcing strength as anomalous fluid pockets move around the thermosyphon.

4.2. Temporal dynamics and flow evolution

The temporal evolution of the flow field can be explored from several fronts. Here we seek to examine and characterize the various thermosyphon flow regimes as the Rayleigh number and associated flow forcing is increased from a conduction state to a high forcing condition. In a time series analysis, we describe the temporal evolution of the bulk mass flow rate in the thermosyphon and then delineate the various flow regimes as a function of the Rayleigh number. We then present and discuss frequency characteristics of the mass flow fluctuations in the thermosyphon and conclude with an analysis of flow reversals and residence time in a given circulatory state.

4.2.1. Time series analysis

The typical progression of flow regimes with increased forcing is as follows: (1) pure-conduction and/or quasi-conduction characterized no bulk circulation around the thermosyphon and weak, localized circulations proximate to the ± heat flux discontinuity (i.e., at $\theta = 0$ and $\theta = \pi$); (2) stable convection characterized by continuous, unidirectional bulk mass-flow (no flow reversals) with oscillations typically decaying to a steady-state value; (3) Lorenz-like chaotic flow characterized by oscillations that grow in amplitude with time and result in flow reversals where the bulk mass-flow transitions from *CCW* to *CW* and back to *CCW* many times throughout a given simulation; and (4) high-Rayleigh, stable convection characterized by unidirectional flow with high frequency, low amplitude, aperiodic oscillations centered about a particular mass flow rate.

Figs. 4–9 present the temporal evolution of the bulk mass flow rate in the thermosyphon as the Rayleigh number is increased from 2.83×10^4 to 2.83×10^7. The Rayleigh number variations in this sequence are obtained by fixing gravity at $9.8\ \mathrm{m/s^2}$ and varying the wall heat flux. Note that in Figs. 4–9 the scale of the ordinate axis (mass flow rate) varies; this is done so as to provide detailed resolution of the oscillatory flow evolution. This progression of flow regimes as the Rayleigh number is increased (Figs. 4–9) is typical for all simulations and is independent of the combination of gravity (g) and heat-flux (q'') that is specified in order to yield a particular value of the Rayleigh number (Ra). As such, the analysis and discussion below pertaining to the particular case of $g = 9.8\ \mathrm{m/s^2}$ is representative for all values of gravity considered.

Stable, damped, asymptotic convection can be seen in Fig. 4 ($Ra \sim 2.83 \times 10^4$) and Fig. 5 ($Ra \sim 1.42 \times 10^5$) where the flow exhibits unidirectional oscillations that decay to a steady-state convective flow regime. Both cases exhibit start-up flow reversals which are a transient residual of the initial condition of the system and is typical behavior observed for all convective regimes. This transient start-up is then followed by stable, unidirectional, non-reversing, decaying oscillations which asymptote to the steady-state value indicated on the figures. In this regime, the Rayleigh number/forcing is sufficiently large so as to maintain steady-state convection, but not large enough to allow instabilities to grow and generate flow reversals.

Chaotic flow regimes are portrayed in Figs. 6–8 where flow oscillations grow in magnitude until a flow reversal occurs. As the Rayleigh number is increased, the oscillatory frequency increases and flow reversals occur more often.

Finally, as the Rayleigh number becomes sufficiently large, as in Fig. 9 with $Ra \sim 2.83 \times 10^7$, we observe unidirectional convection with high-frequency, low amplitude, aperiodic oscillations centered about a mass flow rate of approximately 0.525 kg/s. At sufficiently large Rayleigh numbers, the flow becomes momentum-dominated, the growth of flow instabilities is limited, and thus no reversal occurs. Note that in Fig. 9 we again see several initial, transient flow reversals during start-up before the system settles into the high-Rayleigh, aperiodic, stable convective flow regime.

As a compliment to the flow regime sequence described above, a summary figure of mass flow rate evolution for increasing Rayleigh numbers in thermosyphons operating at $g = 6.0\ \mathrm{m/s^2}$ is shown in Fig. 10. Here, all plots have the same scale on the ordinate axis in order to facilitate direct comparisons of the mass flow magnitude. Simulations with weak forcing (i.e., low Ra) require a longer start-up time, as compared to cases with higher Rayleigh numbers, in order to establish thermal instabilities that are sufficient to generate bulk mass flow in the thermosyphon.

We now demonstrate the sole dependency of the flow on the Rayleigh number. To do so, the results of all parametric cases (i.e., all values of g, q'') have been used to calculate the root-mean-square (*RMS*) value of the mass flow rate as a function of Rayleigh number. This value is shown as a dash-dot line in Figs. 4–9 and approximates the value of the unstable convecting equilibrium solution around which the state oscillates. In Fig. 11 we present a summary plot showing the *RMS* value of mass flow rate as a function of Rayleigh number for each parametric case examined in this study. It is observed that all data collapse onto a single curve. This suggests that the Rayleigh number as defined in Eq. (3) is properly accounting for the forcing in the system due to both gravity and heat flux as they combine to drive the flow around the thermosyphon. An exponential curve-fit is applied to the data as shown in Fig. 11 (regression coefficient of 0.98) and indicates that the *RMS* of mass flow rate scales as $Ra^{0.45}$ which is consistent with power law scalings found in common internal natural convection problems [23].

4.2.2. Frequency analysis

Next, we focus our attention to the frequency characteristics of the flow pulsations observed in the data of Figs. 4–10. Using the mass flow rate as an input signal, power spectra are computed using a Fourier transform for each of the cases. Fig. 12 presents representative power spectra for selected thermosyphon flow regimes. Based on the computational parameters employed in this work (time-step size, data reporting intervals), the power spectra is able to capture frequencies up to 8.0×10^{-2} Hz, which is roughly 1/10 to 1/40 of the time it takes for a pocket of fluid to traverse the circumference of the thermosyphon depending on convective equilibrium flow rates.

Fig. 12(A) corresponds to the mass flow signal observed in Fig. 4 ($Ra \sim 2.83 \times 10^4$) and is representative of the frequency spectrum of convective flow with damped, asymptotic oscillations that decay to stable, steady-state convection. The dominant frequency in the oscillatory mass flow signal is approximately 6.0×10^{-4} Hz; however, note that the peak is not sharp and the peak region is somewhat broad. A relatively low forcing ($Ra \sim 1.73 \times 10^6$), chaotic power spectrum is shown in Fig. 12(B) and corresponds to the mass flow signal of Fig. 10(E). In this case, the peak in the power spectrum occurs at approximately 3.0×10^{-3} Hz and is more pronounced as compared to the lower Rayleigh number cases. As the Rayleigh number is further increased to a moderately high forcing, chaotic flow regime ($Ra \sim 1.04 \times 10^7$), the power spectrum computed from Fig. 10(H) is shown in Fig. 12(C) and exhibits a

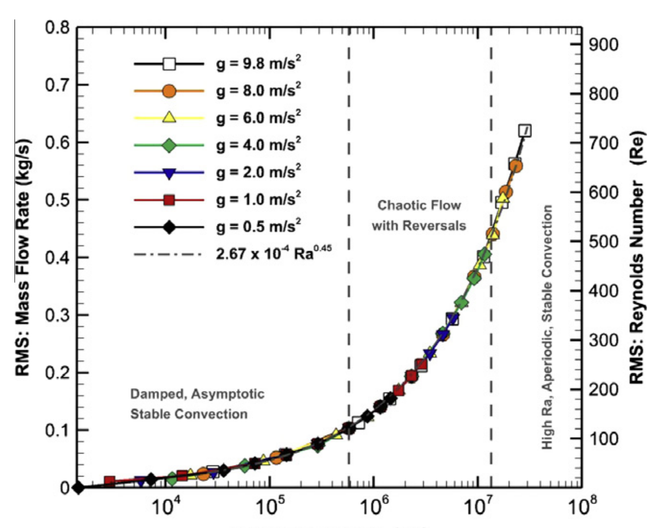

Fig. 11. The root-mean-square (*RMS*) value of mass flow rate (kg/s) in the thermosyphon as a function of the Rayleigh number for varying strengths of the gravitational acceleration. Note that the *RMS* value of mass flow depends on the Rayleigh number and is well-fit by the curve $\dot{m} \sim Ra^{0.45}$.

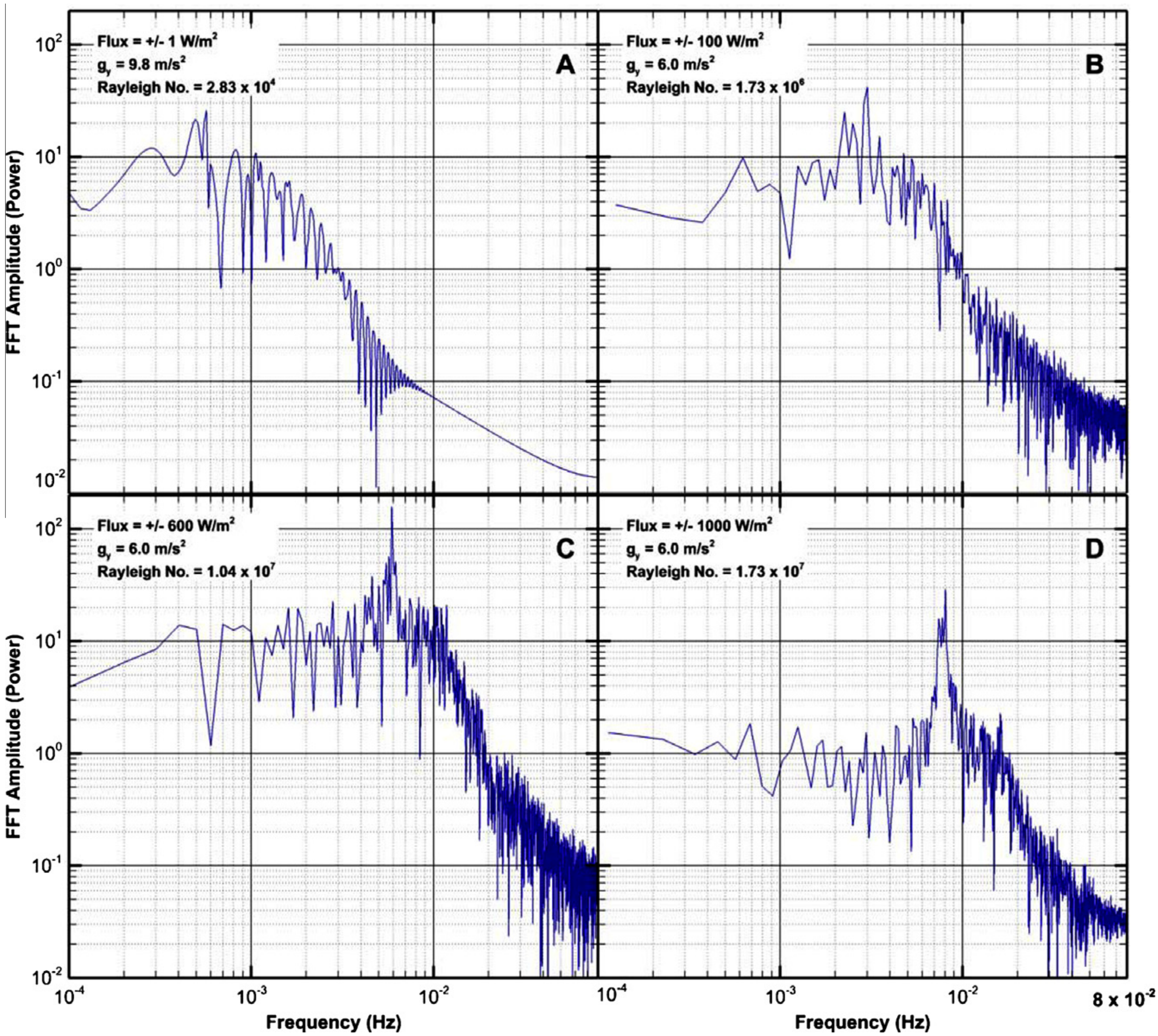

Fig. 12. A summary plot of the FFT power spectrum for selected mass flow evolutions: (A) the stable, oscillatory, decaying flow shown in Fig. 4; (B) the low forcing chaotic flow shown in Fig. 10(E); (C) the high forcing chaotic flow shown in Fig. 10(H); and (D) the high-Rayleigh, aperiodic, stable convective flow shown in Fig. 10(I). Note that the dominant frequency increases with Rayleigh number as the peak becomes more pronounced.

dominant frequency of 6.0×10^{-3} Hz; the spectrum shows an even more prominent peak. Lastly, in Fig. 12(D), the power spectrum for the high-Rayleigh ($Ra \sim 1.73 \times 10^7$), aperiodic, stable convection flow regime computed from Fig. 10(I) is shown. This regime demonstrates the sharpest peak at 8.0×10^{-3} Hz as the low frequencies weaken and the peak shifts even further to the right on the frequency spectrum compared to lower Rayleigh number cases. In general, as the forcing in the thermosyphon increases, the dominant frequency increases and the peak in the power spectrum becomes more pronounced.

To summarize the oscillatory behavior, the dominant frequency has been extracted from power spectra data for each parametric case considered in this study. The dominant frequency is found to exhibit a power law relationship with respect to the Rayleigh number. Specifically, it is found that $f_{\max} \sim Ra^{0.48}$ and is plotted as a function of the Rayleigh number in Fig. 13. The curves exhibit minor disparities for $Ra < 6.0 \times 10^5$ in the damped, asymptotic, stable convection regime but converge and exhibit strong coherence for $Ra > 6.0 \times 10^5$ in both the chaotic and high-Rayleigh, aperiodic, stable regimes.

4.2.3. Flow reversals and residence time

The rate of flow reversals in the thermosyphon (from *CW* to *CCW*, or vice versa) under the various forcing conditions is considered along with measurements of the average time in which the flow resides in a particular direction (*CW*/*CCW*) before experiencing a flow reversal. These two metrics are a representative measure of the chaotic intensity of the thermosyphon operating under a particular set of parameters. In Fig. 14, a plot of the count of flow reversals for the first 10,000 s of flow time is shown as a function of the Rayleigh number and the figure is delineated in terms of flow regime (stable convection, chaotic, and aperiodic stable convection). It is clear that the chaotic nature of thermosyphon flows, as measured by the rate of flow reversals, increases with Rayleigh number up to a critical value.

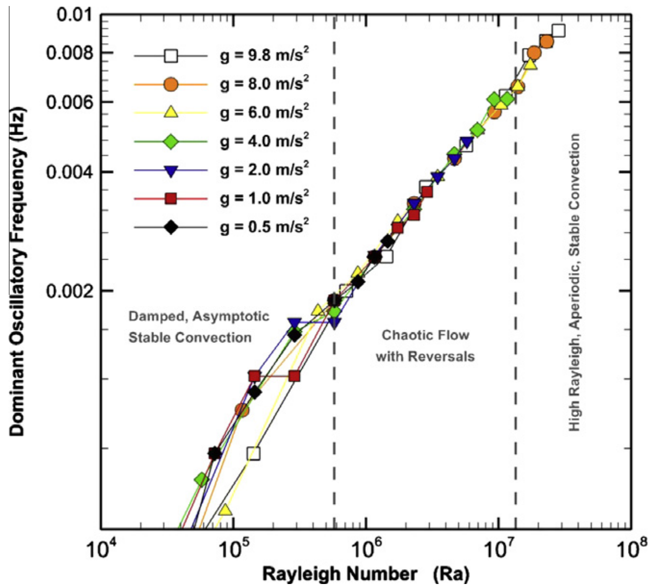

Fig. 13. The dominant oscillatory frequency of the mass flow pulsation magnitude in the thermosyphon. Dominant frequencies are determined by the peak in the power spectra from the Fourier transform of the temporal mass flow evolution. It is found that the dominant frequency scales as $Ra^{0.48}$.

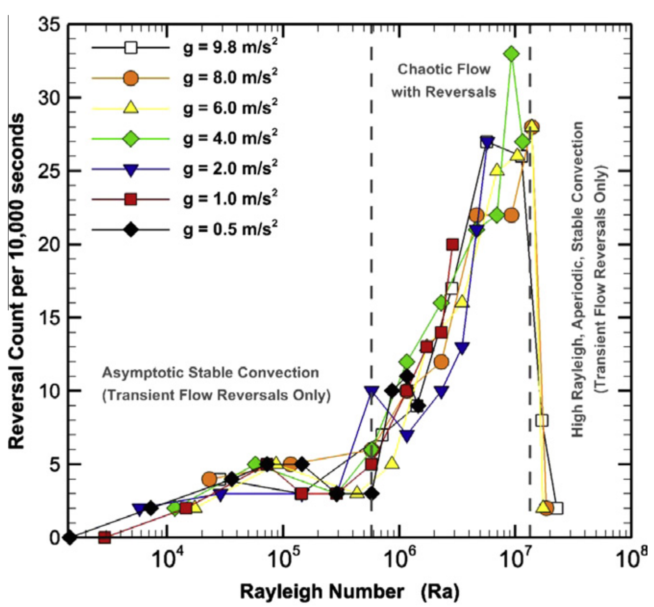

Fig. 14. A count of the number of flow reversals in the thermosyphon for 10,000 s of flow time shown as a function of Rayleigh number. Note the number of flow reversals increases with Ra until the high-Rayleigh, aperiodic, stable regime is realized at which point the number of reversals includes only the transient, start-up reversals which thus accounts for the sharp decline in the number of reversals for $Ra > 10^7$.

However, for Rayleigh numbers above the chaotic flow regime limit ($Ra > 1.7 \times 10^7$), the count of flow reversals drops off sharply. This represents the transition to high-Rayleigh, aperiodic, stable convection in which the flow remains in either the *CW* or *CCW* direction and oscillates aperiodically without reversing. In this case, the flow reversals are 'start-up transients' and occur only during flow start-up after which the forcing is too strong to allow instabilities to grow and generate additional reversals. Similarly, in the case of weak forcing ($Ra < 6.0 \times 10^5$), only transient, start-

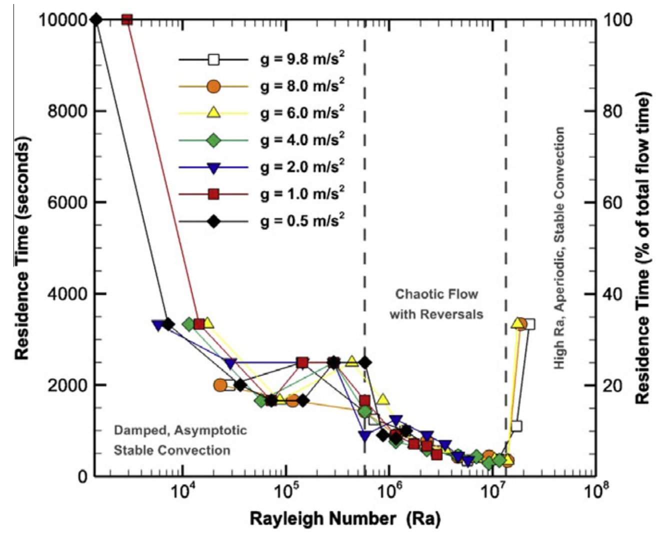

Fig. 15. A plot showing the average time that the flow resides in either a *CW* or *CCW* circulatory direction before reversing as a function of the Rayleigh number during the 10,000 s of flow time.

up reversals are found for cases of stable, damped convection. Here the reversals terminate due to insufficient forcing and the pulsations decay to a steady-state convective regime.

For thermosyphon flows with Rayleigh numbers outside the range of the chaotic regime (i.e., within the stable convection regimes at $Ra < 5.8 \times 10^5$ and $Ra > 1.4 \times 10^7$), the number of flow reversals are solely the result of transient behavior occurring during the start-up period. These transient reversals are a residual artifact of the initial quiescent, isothermal condition of the fluid system as it responds to the applied thermal forcing. Typically, there are between 2 and 5 transient reversals that occur before the flow settles into either a damped, stable convection or a high-Rayleigh, aperiodic, stable convection regime as determined by the strength of the forcing. It is therefore important to distinguish between reversals that occur in a truly chaotic flow regime and continue in perpetuity vs. transient flow reversals that occur only during start-up.

The duration between flow reversals, or residence time, is a measure of the length of time in which the thermosyphon flow field rotates in a particular direction (*CW*/*CCW*) before reversing; it is thus also a measure of stability in convection cells. Here we have calculated the average residence time from the mass flow time series data for each parametric case and the results are plotted in Fig. 15 as a function of Rayleigh number. The chaotic flow regime clearly demonstrates a decreasing value of residence time as the Rayleigh number increases, which is consistent with the increasing frequency of flow reversals in Fig. 10(D)–(H). This result suggests that as the forcing increases, the system becomes less stable and more readily reverses direction. However, as the forcing grows sufficiently large ($Ra > 1.4 \times 10^7$) the system enters the high-Rayleigh, aperiodic, stable regime and the residence time increases accordingly.For thermosyphon flows in the stable convection regimes (i.e., asymptotic, stable convection and the high-Rayleigh, aperiodic, stable convection), it is important to mention that the residence time is an approximate measure of the influence of the initial condition as well as a measure of the rate of start-up transients. As transient reversals occur in relatively large numbers during the start-up of stable flows (see Fig. 14), the calculation of residence time is 'artificially' decreased on a 10,000 s of simulated flow time basis. If the total flow time grows sufficiently large ($\gg$10,000 s) and the system remains in a stable, unidirectional re-

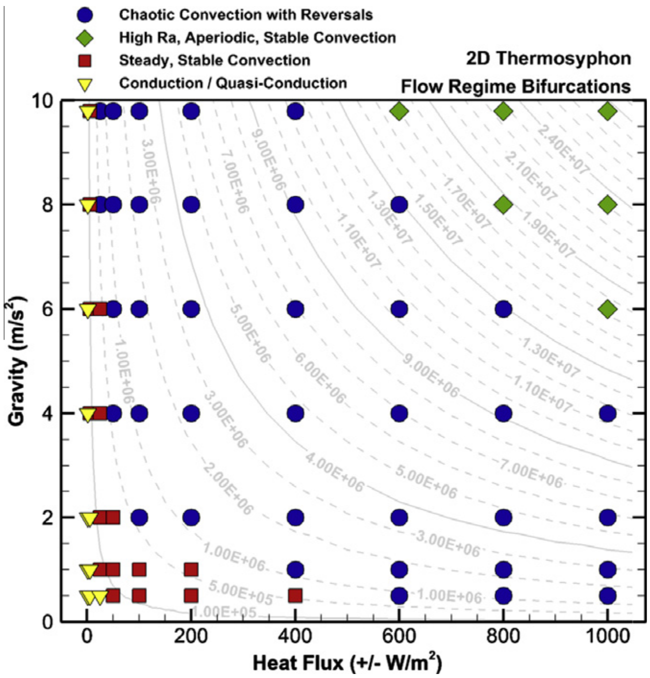

Fig. 16. A flow regime bifurcation diagram as a function of heat flux and gravity with Rayleigh number contour intervals indicated.

gime, (or, if the forcing is sufficiently small as in pure conduction), the residence time will approach 100% of the total flow time. This is reflected in Fig. 15 for Rayleigh number cases falling outside of the chaotic flow regime.

4.3. Flow regime delineation

We close our results and discussion by delineating the various flow regimes as a function of gravity and heat flux input parameters. Fig. 16 shows a flow regime bifurcation diagram in the 2D parametric space of gravity and heat flux with iso-contour lines of the corresponding Rayleigh number. The flow regimes have been characterized for all parametric conditions considered in this study. We have identified a low Rayleigh, pure conduction regime and it is clear that a critical Rayleigh number exists for the onset of convection. While determining this critical Rayleigh number is not the purpose of this work, we mention here that our data suggests pure conduction occurs for $Ra \leqslant 1.5 \times 10^2$ whereas cases with $Ra > 10^3$ exhibit natural convection. Our results further indicate that stable convection generally occurs in the range $10^3 < Ra < 5.8 \times 10^5$, chaotic flow with reversals are observed in the range $5.8 \times 10^5 < Ra < 1.4 \times 10^7$ while high-Rayleigh, aperiodic, stable convection is found for $Ra > 1.4 \times 10^7$. The delineation of flow regimes is necessarily an estimation based on the particular cases and simulation parameters explored in this study. The possibility exists that some flow regimes which appear to be stable convection for flow times up to 10,000 s may in fact have slow-growth instabilities that result in flow reversals that occur over extremely large time periods.

5. Conclusions

In this study, we have numerically modeled a 2D thermosyphon natural convection loop with heat flux boundary conditions. Computational results have been presented which characterize the temporal evolution of the velocity and temperature fields along with the *RMS* value of bulk mass flow rate. Simulation results show that the Rayleigh number has been appropriately recast in terms of the heat flux parameter and thus represents the relevant non-dimensional quantity that accurately captures the physics of the flow for the range of heat flux and gravitational acceleration considered. Over a range of Rayleigh numbers ($1.5 \times 10^2 \leqslant Ra \leqslant 2.8 \times 10^7$), numerical results show that four distinct flow regimes exist: (1) conduction, (2) damped, stable convection that asymptotes to steady-state, (3) Lorenz like chaotic convection with flow reversals, and (4) high-Rayleigh, aperiodic, stable convection.

It has been shown that for sufficiently small Rayleigh numbers, the forcing in the system is small and only conduction occurs. As the Rayleigh number grows slightly larger, a state of stable convection is established. The stable convection may appear in two forms. In the first, the flow exhibits a unidirectional, oscillatory behavior that decays in time and asymptotes to a constant, steady-state bulk mass flow rate. The second form exhibits a unidirectional, oscillatory flow that persists without decay. Chaotic flow regimes are generally observed in the range of Rayleigh numbers from $5.8 \times 10^5 < Ra < 1.4 \times 10^7$ and are characterized by spontaneously occurring flow reversals and/or growing oscillations that yield to flow reversals after an undetermined and inconsistent number of cycles. The frequency of both the oscillations and flow reversals increase with Rayleigh number up to a critical value. At higher Rayleigh numbers ($Ra > 1.4 \times 10^7$), a new regime of stable convection occurs. The high-Rayleigh stable convection regime is characterized by unidirectional, high frequency, low amplitude, aperiodic oscillations. At these high Rayleigh numbers, the forcing is large, the flow-field is momentum-dominated, and instabilities are unable to grow sufficiently large so as to generate flow reversals.

Acknowledgments

This research was supported by a NASA EPSCoR Grant and NSF Grant # DMS-0940271 to CMD as a member of the Mathematics and Climate Research Network. It was also supported by the Vermont Advanced Computing Core and the Vermont Complex Systems Center.

Appendix A. Supplementary data

Supplementary data associated with this article can be found, in the online version, at http://dx.doi.org/10.1016/j.ijheatmasstransfer.2013.02.015.

References

[1] Walker S. Ashley, Thomas L. Mote, Mace L. Bentley, On the episodic nature of derecho-producing convective systems in the United States, Int. J. Climatol. 25 (14) (2005).
[2] Robert H. Johns, William D. Hirt, Derechos: widespread convectively induced windstorms, Weather Forecasting 2 (1987) 32–49.
[3] Ron W. Przybylinski, The bow echo: observations, numerical simulations, and severe weather detection methods, Weather Forecasting 10 (1995) 203–218.
[4] A. Mertol, R. Greif, A review of natural circulation loops, in: S. Kakac et al. (Eds.), Handbook of Natural Convection: Fundamentals and Applications, Hemisphere, Washington, DC, 1985, pp. 1033–1071.
[5] R. Greif, Natural circulation loops, ASME J. Heat Transfer 110 (1988) 1243–1258.
[6] Y. Zvirin, A review of natural circulation loops in pressurized water reactors and other systems, Nucl. Eng. Des. 67 (1981) 203–225.
[7] E.N. Lorenz, Deterministic nonperiodic flow, J. Atmos. Sci. 20 (1963).
[8] K.D. Harris, E.-H. Ridouane, D.L. Hitt, C.M. Danforth, Predicting flow reversals in chaotic natural convection using data assimilation, Tellus Ser. A 64 (2012) 17598.
[9] K.T. Yang, Natural convection in enclosures, in: S. Kakac et al. (Eds.), Handbook of Single-Phase Heat Transfer, Wiley, New York, 1987 (Chapter 13).
[10] G.D. Raithby, K.G.T. Hollands, Natural Convection, third ed., Handbook of Heat Transfer, McGraw-Hill, New York, 1998 (Chapter 4).
[11] Y. Jaluria, Natural Convection, Heat Transfer Handbook, Wiley, New York, 2003 (Chapter 7).

[12] J.B. Keller, Periodic oscillations in a model of thermal convection, J. Fluid Mech. 26 (1966) 599–606.
[13] P. Welander, On the oscillatory instability of a differentially heated fluid loop, J. Fluid Mech. 29 (1967).
[14] M. Gorman, P.J. Widmann, K.A. Robins, Nonlinear dynamics of a convection loop: a quantitative comparison of experiment with theory, Physica D 19 (1986) 255–267.
[15] P.K. Vijayan, Experimental observations on the general trends of the steady state stability behavior of single-phase natural circulation loops, Nucl. Eng. Des. 215 (2002).
[16] Y.Y. Jiang, M. Shoji, M. Naruse, Boundary condition effects on flow stability in a toroidal thermosyphon, Int. J. Heat Fluid Flow 23 (2002) 81–91.
[17] Y.Y. Jiang, M. Shoji, Spatial and temporal stabilities of flow in a natural circulation loop: influences of thermal boundary condition, ASME J. Heat Transfer 125 (2003) 612–623.
[18] G. Desrayaud, A. Fichera, M. Marcoux, Numerical investigation of natural convection in a 2D-annular closed-loop thermosyphon, Int. J. Heat Fluid Flow 27 (2006) 154–166.
[19] H.F. Creveling, J.F. De Paz, J.Y. Baladi, R.J. Schoenhals, Stability characterisitcs of a single phase free convection loop, J. Fluid Mech. 67 (1975) 65–84.
[20] E.H. Ridouane, C.M. Danforth, D.L. Hitt, A 2-D numerical study of chaotic flow in a natural convection loop, Int. J. Heat Mass Transfer 53 (2010) 76–84.
[21] E.H. Ridouane, C.M. Danforth, D.L. Hitt, A numerical investigation of 3-D flow regimes in a toroidal natural convection loop, Int. J. Heat Mass Transfer 5 (2011) 5253–5261.
[22] FLUENT Manual, FLUENT Inc., 10 Cavendish Court, Centerra Resource Park, Lebanon, NH 03766, USA, 2006.
[23] F.P. Incropera, D.P. Dewitt, Fundamentals of Heat & Mass Transfer, fourth ed., John Wiley & Sons, 1996.